Electroosmotic Self-Propelled Microswimmer With Magnetic Steering

Toshiro Yamanaka, *Member, IEEE*, and Fumihito Arai, *Member, IEEE*

***Abstract*—Microswimmers have significant potential for medical applications such as long-term on-demand medication, painless microscale surgery, and so on. The outstanding challenge is to realize power supply, propulsion, and steering mechanisms suitable for operations within the human body and microscale fluids. We propose the microswimmer composed of a self-propulsive disk-shaped module with multiple channels using biofuel cell (BFC) and electroosmotic propulsion (EOP) and a magnetic rod using magnetic steering (MS). The BFC produces an open-circuit potential (OCP) between a bioanode and a biocathode by redox reactions. The EOP generates a self-propulsive velocity due to counteracting forces of electroosmotic flows produced by the OCP in the channels arranged between the electrodes. The MS works by aligning the magnetic rod in a controlled magnetic field direction. The prototype was designed and fabricated using an insulating polymer layer, two conductive layers incorporating silver nanoparticles with anodic/cathodic enzymes, and a magnetic layer containing magnetic nanoparticles. The fast self-propulsion of continuously rotating 30 μm prototypes by the steering in a glucose solution was demonstrated as expected theoretically. This concept has the potential to be used as microrobots for future medical applications such as a pulling mechanism to assist in guidewire insertion or agents delivering drugs.**

***Index Terms*—Micro/nano robots, microswimmer, biofuel cell, electroosmotic flow, magnetic steering.**

I. Introduction

BIOMEDICAL swimming microrobots are expected to have innovative and noninvasive medical applications, such as long-term on-demand medication, painless microscale surgery, single-cell level diagnosis, cell-mimicking detoxification, and so on [1], [2], [3], [4]. Microrobots have been discussed that autonomously move within the human body through the blood-vascular system and carry out various medical missions [1], [2], [3]. Such microrobots require microscale mechanisms such as energy supply, propulsion, control, navigation, communication, and manipulation. Energy supply and propulsion mechanisms through biofluids are the most essential challenges. These mechanisms should utilize energy conversion and propulsion that can effectively work within microscale regions of the human body. Additionally, robots capable of movement within blood vessels against flow velocity and fluid torque are ideal because they can reach most tiny spaces within the body and perform a variety of missions requiring access to specific targets. More particularly, mechanisms movable against capillary flows require a size of several 10 μm or less and propulsion velocities of several 100 μm/s or more [1].

Numerous microscale propulsion mechanisms have been developed, including external-fields-powered propulsions [5], [6], [7], [8], [9], [10], microorganism-powered propulsions [11], and catalytic self-propulsions [12], [13], [14], [15] by bubbles and/or phoretic flows. Conventional mechanisms generally have potential issues with energy supply and fast propulsion in the body. External magnetic fields are useful as a propulsion source because they can penetrate the entire human body [6]. Various motion control methods for small magnetic robots are also being studied [16], [17], [18]. However, magnetically propelled microswimmers require a larger magnetic field and its gradient due to their smaller size. Control systems steering and propelling microswimmers with magnetic fields alone tend to be complex and large.

We have proposed the new concept of the self-propelled tube-shaped microswimmer using biofuel cell (BFC) and electroosmotic propulsion (EOP) [19]. In the BFC mechanism, an open-circuit potential (OCP) is produced by decomposing biofuels such as glucose and oxygen that can be supplied within the human body. In the EOP mechanism, self-propulsion velocity is caused by a counteraction of electroosmotic flow (EOF), with the OCP as the energy source. According to the derived theoretical EOP model, its self-propulsion velocity is proportional to the OCP regardless of the tube size and inversely proportional to the tube length. Therefore, faster self-propulsion velocity can be expected with smaller tube size for the microswimmer using both BFC and EOP mechanisms. This notable feature makes this concept a feasible solution to those requirements. We demonstrated the self-propulsions of 100 μm prototypes [19] with several 10 μm/s velocity and 10 μm prototypes [20] with more than 100 μm/s velocity in a glucose solution. Thus we proved the concept and the smaller and faster feature. However, it did not include the steering function required to propel against the fluid torque.

In this research, we report a new concept of a self-propelled microswimmer using EOP and BFC with magnetic steering.

Manuscript received 18 July 2023; accepted 12 November 2023. Date of publication 29 November 2023; date of current version 8 December 2023. This letter was recommended for publication by Associate Editor T. Xu and Editor X. Liu upon evaluation of the reviewers' comments. This work was supported in part by the "Japan Society for the Promotion of Science" (JSPS) Grants-in-Aid for Scientific Research (KAKENHI) under Grant JP21K18696, and in part by JST Moonshot R&D - MILLENNIA Program under Grant JPMJMS2214-15. *(Corresponding author: Toshiro Yamanaka.)*

The authors are with the Department of Mechanical Engineering, School of Engineering, The University of Tokyo, Tokyo 113-8656, Japan (e-mail: yam104@g.ecc.u-tokyo.ac.jp; arai-fumihito@g.ecc.u-tokyo.ac.jp).

This letter has supplementary downloadable material available at https://doi.org/10.1109/LRA.2023.3337706, provided by the authors.

Digital Object Identifier 10.1109/LRA.2023.3337706

IEEE Robotics and Automation Letters (RA-L) paper, presented at ICRA 2024, Yokohama, Japan. Cite as RA-L paper.

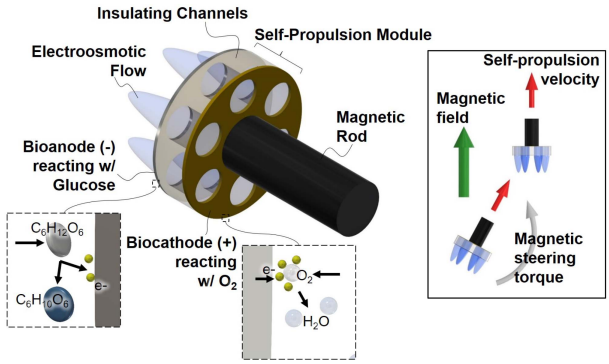

Fig. 1. Concept of electroosmotic self-propelled microswimmer with magnetic steering.

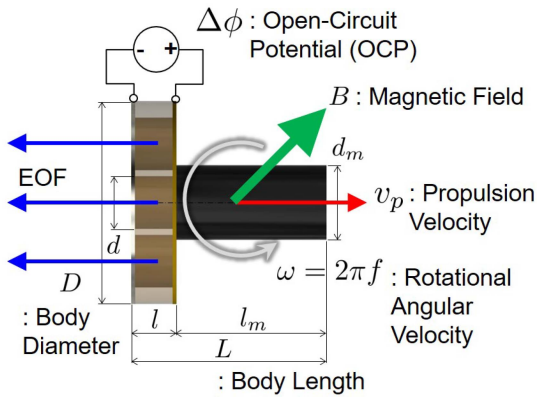

Fig. 2. Main parameters.

This concept satisfies the requirements of fast self-propulsion and steering. We established design and performance estimates based on theoretical models derived for the propulsion velocity and steering angular velocity. Then we evaluated self-propulsion velocity of fabricated prototypes during rotation by steering experimentally to prove the validity of the concept.

II. Concept Description

A. Concept

Fig. 1 shows the concept of the microswimmer using EOP and BFC mechanisms with magnetic steering. This microswimmer consists of a disk-shaped self-propulsion module with multiple through-holes and a magnetic rod. The self-propulsion module includes BFC and EOP mechanisms. The BFC consists of a redox-electrode pair. One electrode acts as a bioanode to oxidize glucose, while the other acts as a biocathode to reduce oxygen. In the BFC mechanism, the redox reactions produce an OCP between the electrodes. The EOP consists of multiple electrically insulating channels placed between them. Electric force by the OCP causes a plug flow of electrolytes within each channel (i.e., EOF). The total counteracting force in the multiple channels then drives the swimmer in the opposite direction of the EOFs. Due to the EOF characteristics, this EOP mechanism can work effectively in microscale fluids. The magnetic rod is soft magnetic [21] and cylindrical in shape. When a uniform magnetic field is applied to it, magnetic torque is generated according to the difference between the directions of the magnetic field and the cylindrical axis. The rod then rotates to align with the direction of the magnetic field. Thus the swimmer can then be steered in that direction. If a microswimmer is not only steered but also propelled by a magnetic field, a smaller one requires a larger magnetic field and its gradient. There is a trade-off relationship between the workspace and the propulsion velocity due to the force [6], and the number and size of the coils generating the magnetic field increase, making its whole system more complex. Our concept uses EOP and magnetic steering with only a uniform magnetic field, which simplifies the system compared to the magnetic propulsion method.

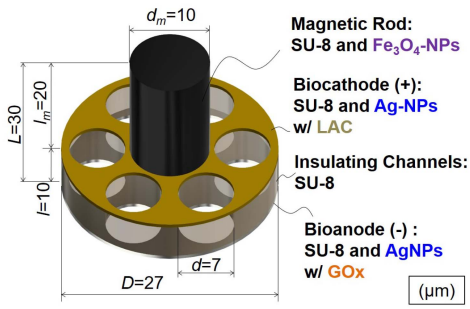

Fig. 3. Configuration and design.

B. Configuration and Parameters

The details of main parameters are given in Fig. 2. L, l, and l_m are the lengths of the total body, the insulating channels, and the magnetic rod, respectively. D, d, and d_m are the diameters of the body, the channel, and the rod, respectively. $\Delta\phi$ is the OCP generated by the BFC. Self-propulsion velocity v_p is generated along the body axis at the center of gravity (CG). Rotational angular velocity ω is generated at the CG depending on the difference between directions of magnetic field B and v_p. The body axis is aligned synchronously with the direction of the external magnetic field B with $\omega = 2\pi f$. f is the steering frequency.

The design and configuration are shown in Fig. 3. The layer of the insulating channels was made from the UV-curable photoresist SU-8 suitable for photolithography. The bioanode and biocathode were made of conductive polymer composites (CPCs) [20] incorporating SU-8 and enzyme-immobilized silver nanoparticles (AgNPs). Glucose oxidase (GOx) was used as the anodic enzyme and laccase (LAC) as the cathodic enzyme. GOx promotes the reaction with glucose and LAC with oxygen. The magnetic rod was made of magnetic polymer composites (MPCs) [22], [23] incorporating SU-8 and magnetic nanoparticles (MNPs). Magnetite nanoparticles (Fe_3O_4NPs) were used as MNPs. The outer size (D, L) of the body was set to about 30 μm as the minimum value that can be fabricated by UV mask photolithography. All parameters are summarized in Table I.

IEEE Robotics and Automation Letters (RA-L) paper, presented at ICRA 2024, Yokohama, Japan. Cite as RA-L paper.

TABLE I
PARAMETERS

Meaning	Part	Symbol	Value (Units)	Material
Boltzmann constant	-	k_B	1.38×10^{-23} (J/K)	-
Tempereture	-	T_0	310 (K)	-
Permeability	Free space	μ_0	$4\pi\times10^{-7}$ (T m/A)	-
Permittivity	Fluid	ε	6.580×10^{-10} (F/m)	Water
Viscosity	Fluid	η	0.692 (mPa s)	Water
Mass density	Fluid	ρ_f	993 (kg/m^3)	Water
Mass density	Insulating channels	ρ	1190 (kg/m^3)	SU-8 [24]
Zeta potential	Insulating channels	ζ	-30 (mV)	SU-8 [25]
OCP	BFC	$\Delta\phi$	200 – 400 (mV)	[19], [26]
Diameter	Swimmer	D	27 (μm)	-
Length	Swimmer	L	30 (μm)	-
Diameter	Channel	d	7 (μm)	-
Number	Channel	n	6 (-)	-
Length	Self-propulsion module	l	10 (μm)	-
Length	Magnetic rod	l_m	20 (μm)	-
Diameter	Magnetic rod	d_m	10 (μm)	-
Saturation magnetization	MNP	M_s	$0.6/\mu_0$ (A/m)	Fe_3O_4 [27]
Diameter	MNP	d_{MNP}	10 (nm)	Fe_3O_4NP [27]
MNP concentration in polymer	MPC	α_{MNP}	7 (Vol%)	Fe_3O_4NP in SU-8
Magnetic field	Free space	$\lvert B\rvert$	≤ 6 (mT)	-

C. Theoretical Model of Biofuel Cell

The BFC function is performed by a bioanode with GOx and a biocathode with LAC. On the electrodes, the redox reactions occur as follows [19]:

$$(\text{Bioanode}): \underbrace{C_6H_{12}O_6}_{\text{Glucose}} \xrightarrow{\text{GOx}} C_6H_{10}O_6 + 2H^+ + 2e^-, \quad (1)$$

$$(\text{Biocathode}): \frac{1}{2}O_2 + 2H^+ + 2e^- \xrightarrow{\text{LAC}} H_2O. \quad (2)$$

By the above reactions, the OCP $\Delta\phi$ is generated between the electrodes. Therefore, this swimmer can be supplied with energy in fluids containing glucose and oxygen, such as biological fluids. The Gibbs free energy of the reactions provides a theoretical suppremum for the OCP, with an estimated value of 1.18 V [28], and the OCP is independent of the electrode size. We have confirmed an OCP of 200–400 mV using test substrates [19] and film-shaped prototypes [26] with the same configuration.

D. Theoretical Model of Electroosmotic Self-Propulsion

The EOF reaction force is much larger than the drag force acting on the outer surface as theoretically proved in [19]. Therefore, the outer drag force is negligibly small, and momentum conservation stands between the swimmer (with the mass of m and the velocity of v_p) and the inner bulk electrolyte inside all channels (with the mass of m_f and the velocity of u_{eo}) as follows:

$$mv_p + m_f u_{eo} = 0. \quad (3)$$

Their relative velocity is equal to the so-called EOF velocity as follows: [29]

$$u_{r,eo} = u_{eo} - v_p = \frac{\varepsilon\zeta}{\eta}\frac{\Delta\phi}{l} \quad (4)$$

where ζ is the charged potential of the inner surface of the channels (so-called "zeta potential"). ε and η are the permittivity and viscosity of the electrolytic solution.

Self-propulsion velocity model v_p of the swimmer can be derived from (3) and (4) as follows: [19]

$$v_p = -\frac{1}{1+m/m_f}\frac{\varepsilon\zeta}{\eta}\frac{\Delta\phi}{l}, \quad (5)$$

$$\frac{m}{m_f} = \frac{\rho}{\rho_f}\left\{\frac{D^2}{nd^2}\left(1+\frac{l_m d_m^2}{lD^2}\right)-1\right\}, \quad (6)$$

where ρ and ρ_f are the mass densities of the swimmer and the electrolyte, respectively. $n = 6$ is the number of channels. $(1+m/m_f)^{-1}$ means the conversion rate from the EOF velocity $u_{r,eo}$ to the self-propulsion velocity v_p. The minimized volume and small mass density ρ are effective in increasing $(1+m/m_f)^{-1}$. From (5), faster v_p is clearly expected by thinner length l. The swimmer of previous work [19] was tube-shaped and it has a smaller and faster effect [20]. Disc-shaped Self-propulsive module has also a thinner and faster effect. Therefore, the proposed propulsion mechanism is theoretically suitable and advantageous for use as the self-propulsive microrobot.

E. Theoretical Model of Magnetic Steering

Assuming planar movements of the swimmer, the trajectory radius R is proportional to the ratio of the propulsion velocity v_p to the steering frequency f as follows:

$$R = \frac{v_p}{2\pi f}. \quad (7)$$

Steering frequency f is determined from the equilibrium between magnetic torque T [21] and hydrodynamic torque [30] as follows:

$$f = \frac{|T|}{2\pi\zeta_r}, \quad \zeta_r \simeq \pi\eta D^3, \quad (8)$$

$$T = \Omega_m M \times B, \quad \Omega_m = \frac{\pi}{4} l_m d_m^2, \quad (9)$$

where ζ_r, B, M and Ω_m are hydrodynamic torque coefficient, magnetic field, magnetization and the volume of the magnetic rod, respectively. The magnetic field was assumed to be uniform inside the rod. For (8), ζ_r for a sphere of diameter D was approximately used.

Magnetization of soft magnetic material is described as follows [31]:

$$M = (N + 2\lambda I)^{-1} B/\mu_0 \quad (10)$$

$$\lambda : B^T (N + 2\lambda I)^{-2} B - \mu_0^2 m_s^2 = 0 \quad (11)$$

λ is a Lagrange multiplier minimizing magnetic energy. Fe_3O_4NPs are regarded as superparamagnetic [21] without hysteresis, and the upper limit m_{max} of magnetization of the composite with them is described by the Langevin equation [21], [27] as follows:

$$m_s = \alpha_{MNP} M_s \left(\coth(\alpha|B|) - \frac{1}{\alpha|B|}\right) \quad (12)$$

$$\alpha = \frac{\pi d_{MNP}^3}{6}\frac{M_s}{k_B T_0}$$

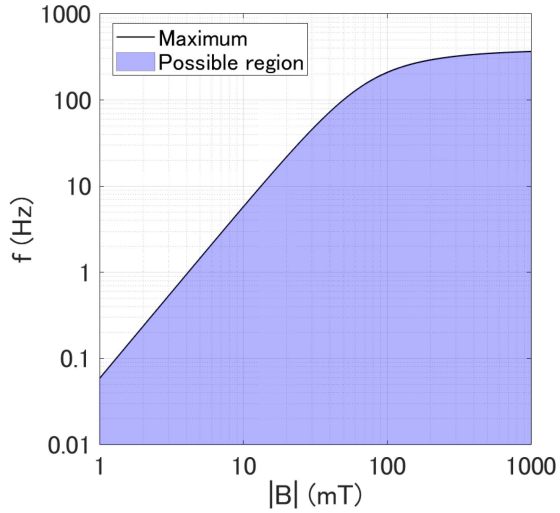

Fig. 4. Theoretical estimates of the maximum steering frequency f that can be generated by the magnitude of the magnetic field B.

TABLE II
THEORETICAL PERFORMANCES

Meaning	Symbol	Value (Units)	Condition
Velocity conversion ratio	$(1+m/m_f)^{-1}$	0.28 (–)	
Relative EOF velocity	$\lvert u_{r,eo}\rvert$	571–1141 (μm/s)	$\Delta\phi$=200–400 (mV)
Self-propulsion velocity	$\lvert v_p\rvert$	159–318 (μm/s)	
Max. steering frequency	f_{max}	2.1 (Hz)	$\lvert B\rvert \leq 6$ (mT)
Min. trajectory radius	R_{min}	12–24 (μm)	

Demagnetizing tensor N can be calculated assuming a magnetically equivalent ellipsoid [32] to the cylinder with $l_m/d_m = 2$ as follows:

$$N = diag(0.4091, 0.4091, 0.1819) \tag{13}$$

To generate magnetic torque, the magnetic object must be asymmetric along the rotation axis. A slender cylinder like this design is effective for magnetic torque due to its asymmetry and for self-propulsion velocity due to its small mass. Using (8)–(13) and parameters in Table I, the maximum steering frequency f that can be generated by the magnitude of the magnetic field B was theoretically estimated as shown in Fig. 4.

F. Performance Estimates

Theoretical performances are summarized in Table II. Assuming $\Delta\phi$ = 200–400 mV [19], [26], the relative EOF velocity $u_{r,eo}$ is estimated to be 571–1141 μm/s by (4). Under these conditions, about 28% of the $u_{r,eo}$ is converted to v_p, which is expected to be 159–318 μm/s by (5) and (6). The small distance between the electrodes contributed to large $u_{r,eo}$ and the volume-minimized body contributed to large $(1 + m/m_f)^{-1}$. Considering a tube-shaped swimmer with the same length of 30 μm, its propulsion velocity is calculated to be 76–152 μm/s. Therefore, the disk-shaped design with a rod is superior to the previous tube-shaped design.

The maximum of the steering frequency $f_{\max}$ is estimated as several Hz under a magnetic field of several mT as shown in Fig. 4. Even if the magnetic field $|B|$ is increased above 100 mT, a few 100 Hz is the upper limit of the steering frequency due to the magnetization saturation of Fe_3O_4NPs. When assuming motion against the flow in the vessel, a rotational angular frequency disturbance due to maximum fluid torque [30] acts on the swimmer near the wall surface. These estimates can be used to determine the required steering frequency and magnetic field due to those environmental conditions. In this paper, we used f_{max} = 2.1 Hz under $|B| \leq 6$ mT. In that case, the minimum trajectory radius $R_{\min}$ is estimated to be 12–24 μm by (7).

From the above, the design of this concept is considered to meet the requirements of fast self-propulsion and steering.

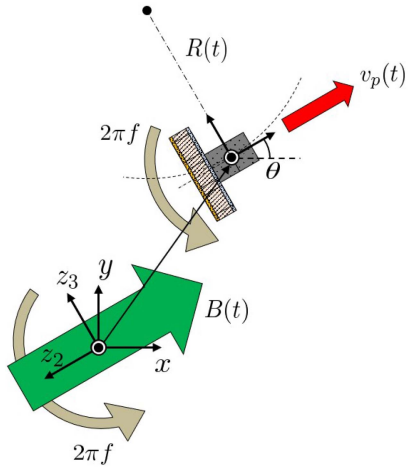

Fig. 5. Planar moving system.

G. Position Control Possibility

Assuming a simple planar moving system with no disturbances, we consider the possibility of position control by this concept. The system shown in Fig. 5 can be described as following the kinematic model:

$$\frac{d}{dt}\begin{bmatrix} x \\ y \\ \theta \end{bmatrix} = \begin{bmatrix} \cos\theta & 0 \\ \sin\theta & 0 \\ 0 & 1 \end{bmatrix} \begin{bmatrix} v_p \\ 2\pi f \end{bmatrix} \tag{14}$$

x, y, and θ represent the swimmer's position and rotation angle in the plane, respectively. v_p is assumed to be non-adjustable, so f is the only input to stabilize position x, y. It is assumed that x, y, θ, and v_p at each time can be identified from imaging methods such as the microscope.

The driftless system (14) is mathematically equivalent to a two-wheeled vehicle moving straight ahead with no brakes and only steering, which is uncontrollable by linear approximation. It can be transformed into the chained form [33] as follows:

$$\frac{d}{dt}\begin{bmatrix} z_1 \\ z_2 \\ z_3 \end{bmatrix} = \begin{bmatrix} 1 & 0 \\ 0 & 1 \\ z_2 & 0 \end{bmatrix} \begin{bmatrix} \nu_1 \\ \nu_2 \end{bmatrix}, \tag{15}$$

where the state vector z and input vector ν are as follows:

$$z = \begin{bmatrix} z_1 \\ z_2 \\ z_3 \end{bmatrix} = \begin{bmatrix} \theta \\ -(x\cos\theta + y\sin\theta) \\ -x\sin\theta + y\cos\theta \end{bmatrix}, \tag{16}$$

$$\nu = \begin{bmatrix} \nu_1 \\ \nu_2 \end{bmatrix} = \begin{bmatrix} 2\pi f \\ -(v_p + z_3 \cdot 2\pi f) \end{bmatrix} \tag{17}$$

Although there are various solutions for the chained form, the control method can be used by transforming it into the time-state control form [34], [35] as follows:

$$\frac{dz_1}{dt} = \mu_1 \tag{18}$$

$$\frac{d}{dz_1}\begin{bmatrix} z_3 \\ z_2 \end{bmatrix} = \begin{bmatrix} 0 & 1 \\ 0 & 0 \end{bmatrix}\begin{bmatrix} z_3 \\ z_2 \end{bmatrix} + \begin{bmatrix} 0 \\ 1 \end{bmatrix}\mu_2 \tag{19}$$

$$\mu = \begin{bmatrix} \mu_1 \\ \mu_2 \end{bmatrix} = \begin{bmatrix} 2\pi f \\ -\left(\frac{v_p}{2\pi f} + z_3\right) \end{bmatrix}, \tag{20}$$

where (18) is the time-control part, (19) is the state-control part with the rotation angle $z_1 = \theta$ as the virtual time scale, and μ in (20) is the new input vector for each part. Equation (19) is linear, so the position feedback controller for f can be designed as follows:

$$f_d = \frac{v_p}{2\pi R_d} \tag{21}$$

$$R_d = sign(f)k_2 z_2 + (k_3 - 1)z_3 - k_3 R_{min}, \tag{22}$$

where the subscripts "d" and "min" represent the desired value and minimum value, respectively. $k_2, k_3 > 0$ are the feedback gains. Fig. 6 shows numerical simulation results of position feedback control to stabilize the swimmer toward the origin by (7), (14)–(22). In the initial state, the swimmer increases the trajectory radius R at a small steering frequency f for a large movement. In the final state, it minimizes R at the maximum f and it continues to rotate around the origin. Thus, position control is theoretically possible.

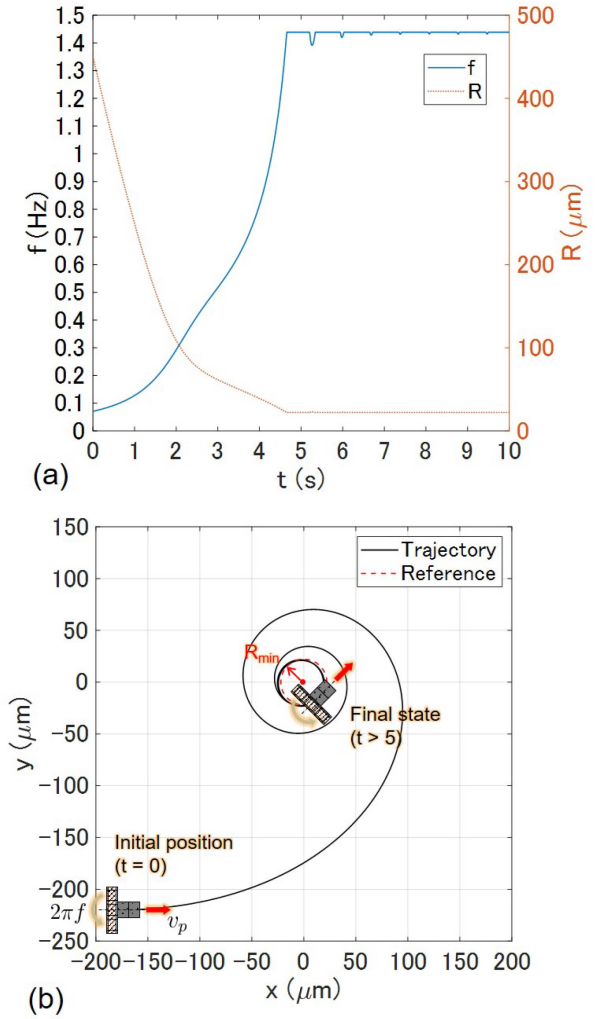

Fig. 6. Numerical simulation results of position feedback control under conditions of $v_p = 200$ μm/s, sampling time=10 ms, $f_{max} = 1.43$ Hz, $R_{min} = 22$ μm, $k_2 = 1.415$, and $k_3 = 0.100$. (a) Time series results of feedback input frequency f and trajectory radius R. (b) Planar trajectory stabilizing to the origin by feedback input f.

III. Proof of Concept

A. Prototype

Fig. 7 shows the fabrication process of prototypes. First, enzymes (GOx or LAC) were covalently immobilized on the surface of AgNPs (Fig. 7(a1)) to facilitate direct electron transfer, and CPC was prepared by dispersing the enzyme-immobilized AgNPs in uncured SU-8 (Fig. 7(a2)) [20], [26]. MPC was also prepared by dispersing Fe_3O_4NPs in uncured SU-8 (Fig. 7(b)). As in the previous research [19], [26], prototypes were fabricated by pattern transfer with UV mask photolithography using the prepared CPCs and MPC. In the photolithography process (Fig. 7(c)), a sacrificial layer made of dextran was coated on a glass substrate. An anodic CPC layer was spin-coated onto the glass substrate, and the pattern of the self-propulsion module shown in Fig. 3 was transferred to it. The same pattern was transferred to an SU-8 layer and a cathodic CPC layer in turn. The rod pattern was then transferred to an MPC layer. All subsequent processes required a baking temperature of less than 65 °C to avoid deactivation of the enzymes [36]. Finally, through chemical development and cleaning, 30 μm prototypes on the substrate were obtained. A top view of a fabricated prototype by optical microscopy is shown in Fig. 8. However, the fabrication yield was not good, because this design was the smallest size that could be fabricated by UV mask photolithography. Also, the channel diameter was 3–4 μm, which was smaller than the nominal value of 7 μm.

B. Experimental Setup

Fig. 9 shows the experimental setup for evaluating the mobility of the fabricated prototypes in glucose solution. A Helmholtz coil system was used to generate a uniform rotating magnetic field in the xy plane. The desired magnetic field can be generated by applying current to the Helmholtz coil system via a computer, real-time controller, DA converters, and bipolar amplifiers. Using a microscope and camera, the mobility of the prototype on the surface of a dish immersed in glucose solution (67 mM β-D-glucose and 150 mM NaCl in 10 mM, 7.4 pH phosphate buffered saline (PBS)) can be observed and verified. All experiments were performed at room temperature of approximately 27 °C.

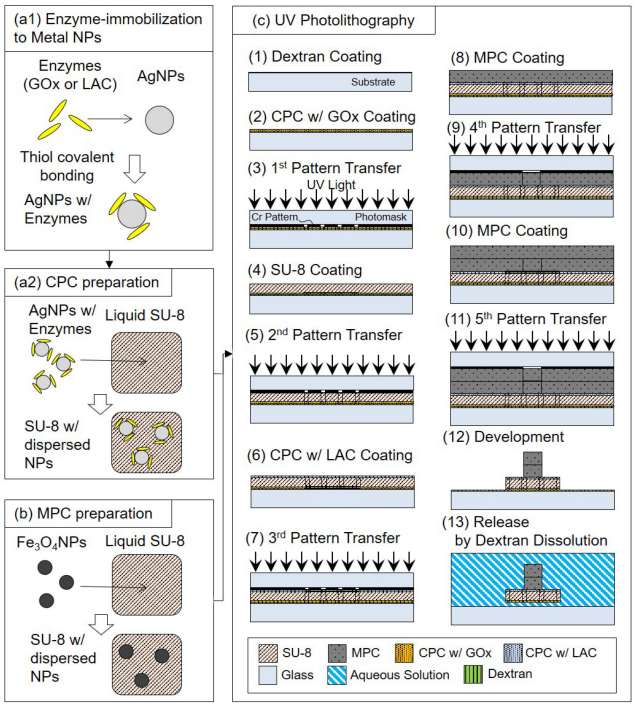

Fig. 7. Fabrication process. (a1) Enzyme-immobilization to metal NPs by covalent bonding method. (a2) CPC preparation by dispersing the enzyme-immobilized metal NPs in uncured SU-8. (b) MPC preparation by dispersing MNPs in uncured SU-8. (c) UV photolithography.

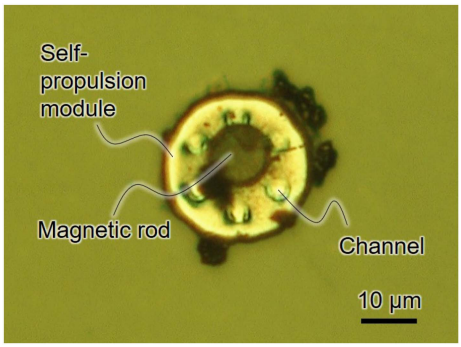

Fig. 8. Top view image of a fabricated prototype by an optical microscope.

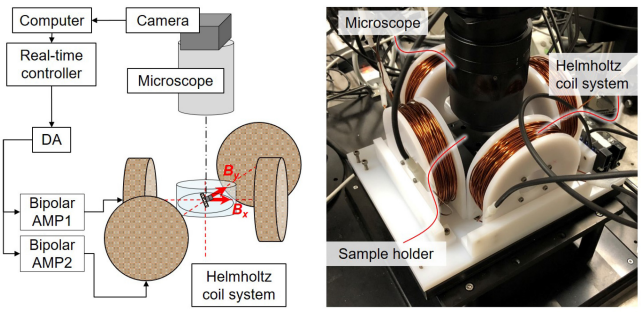

Fig. 9. Setup for the PoC experiments.

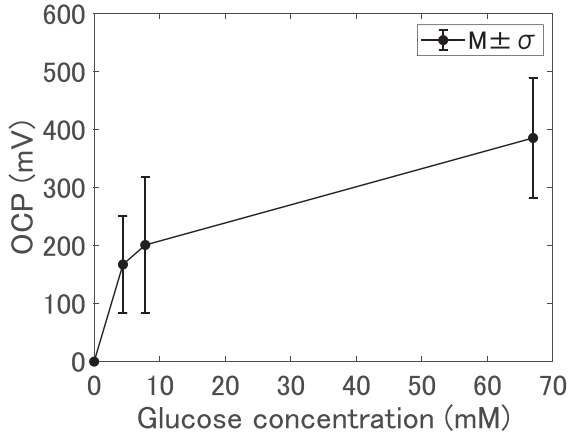

Fig. 10. Measured OCP according to glucose concentration using film-shaped prototypes [26]. The points and bars represent the mean (M) and standard deviation (σ) of OCP time series data continuously generated for more than 30 s by three film-shaped prototypes, respectively.

C. *Preliminary BFC Evaluation for Glucose Concentration*

Using the film-shaped prototypes developed in the previous research [26], we measured OCP in response to glucose solutions (β-D-glucose, 150 mM NaCl in 10 mM, 7.4 pH phosphate buffered saline (PBS)) of different concentrations. The BFC electrodes of those prototypes were fabricated using the same process as shown in Fig. 7. The tested glucose concentrations of 4 mM, 8 mM, and 67 mM are approximately the same as those in the blood of human adults (median) and diabetic patients (lower and upper limits), respectively [1]. Fig. 10 shows the mean and standard deviation of OCP time series data continuously generated for more than 30 s by three film-shaped prototypes, depending on the glucose concentrations. At each concentration, OCP fluctuated significantly with a standard deviation of approximately 100 mV. Even at concentrations of 4 mM and 8 mM, the mean OCP value was approximately 200 mV. The mean OCP value increased gently with concentration, reaching approximately 400 mV at a concentration of 67 mM. From the above, the BFC of this concept has the potential to generate OCP in adult human biological fluids. In subsequent experiments, we adopted a glucose concentration of 67 mM as the maximum value in vivo.

D. *"proof-of-Concept" (PoC) Experiment*

Using the prototypes (Fig. 8) and the experimental setup (Fig. 9), we carried out experiments to evaluate their self-propulsion velocity during magnetic rotation. As mentioned earlier, the fabrication yield was very low and there were few prototypes with self-propulsion, but we could confirm several self-propelled prototypes while rotating at a constant steering frequency $f = 2$ Hz. One prototype in Fig. 11(a) showed rotations with relatively stable v_p and R. Fig. 11(a1) shows the snapshots extracted from an acquired movie for 1.0 s. The red points and white curves added by "OpenCV" represent the CG and its trajectory, respectively. Fig. 11(a2) is the trajectory plot of the prototype CG for 10 s. Fig. 11(a3) shows the identified

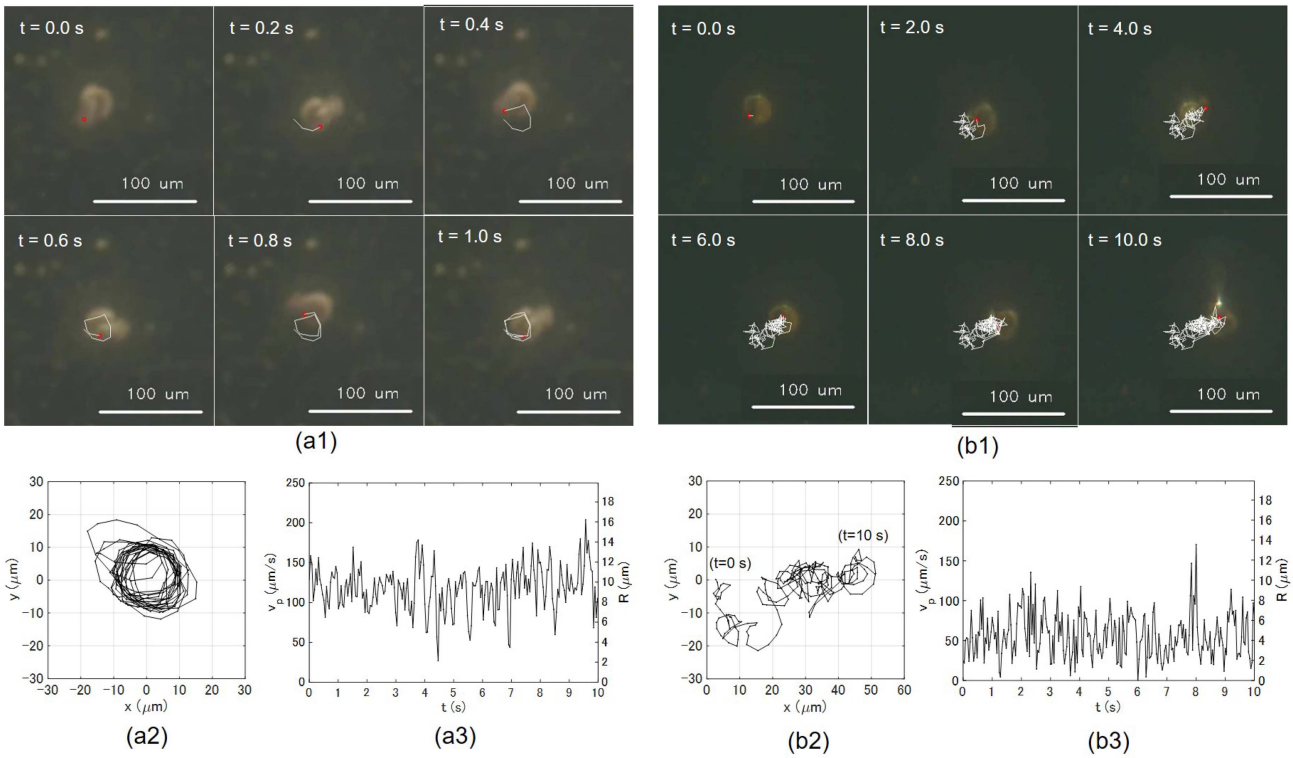

Fig. 11. Experimental results of moving prototypes with constant steering frequency $f = 2$ Hz in 67 mM glucose solution. For all data, the sampling time was 50 ms and moving mean processing was performed for 4 points. (a1)–(a3) Rotations with relatively stable v_p and R of one prototype. (b1)–(b3) Rotations with translations of another prototype. (a1),(b1) Snapshots of the moving prototype. The red points and white curves added by "OpenCV" represent the CG and its trajectory, respectively. (a2),(b2) Trajectory of the prototype CG for 10 s. (a3),(b3) Propulsion velocity v_p and trajectory radius R of the prototype CG for 10 s.

self-propulsion velocity v_p and the corresponding trajectory radius R for 10 s. Another prototype in Fig. 11(b) showed rotations with random translations. Fig. 11(b1) shows the snapshots extracted from an acquired movie for 10.0 s. Fig. 11(b2) is the trajectory plot of the prototype CG for 10 s. Fig. 11(b3) shows the identified self-propulsion velocity v_p and the corresponding trajectory radius R for 10 s.

IV. Discussion

As shown in Fig. 11(a1),(a2), relatively stable self-propulsion with magnetic rotations was observed for 10 s. Mean trajectory radius and mean self-propulsion velocities were identified as 9.4 μm and 118 μm/s, respectively (Fig. 11(a3)). This velocity is comparable to the maximum velocity of the 10 μm tube-shaped microswimmer demonstrated in the previous research [20]. Thus, this microswimmer concept for fast self-propulsion velocity and magnetic steering was demonstrated. The reason for the decrease in velocity relative to the theoretically expected velocity 159–318 μm/s is not clear but might be due to the channel diameter of 3–4 μm smaller than the nominal value of 7 μm. Random translations with magnetic rotations were also observed as shown in Fig. 11(b1),(b2). This is due to self-propulsion velocity fluctuations under the constant rotational frequency because there were no other convective flows in the surrounding environment. The mean and maximum self-propulsion velocity were identified as 56 μm/s and 170 μm/s, respectively (Fig. 11(b3)). Corresponding trajectory radius (mean 3.9 μm, maximum 11.8 μm) varied with the unstable self-propulsion velocity and constant steering frequency. Then, the trajectory radius variations generated the random translations. Although this behavior was caused by open-loop inputs with the constant magnetic rotational frequency, it suggests the position feedback control possibility by changing the trajectory radius, as described in the subsection II-G. The unstable self-propulsion velocity might be due to the OCP and zeta potential of EOP channels. The next challenge is to improve the fabrication yield in order to enhance its velocity stability. Instead of the mask lithography used in this research, two-dimensional direct laser writing lithography or two-photon absorption polymerization lithography [20] by three-dimensional scanning of a femtosecond laser are considered suitable for higher fabrication yield, and are the next solutions to be performed.

V. Conclusion

In this research, we proposed a new concept of a self-propelled microswimmer using EOP and BFC with magnetic steering. We established design and performance estimates based on theoretical models. Then we proved the validity of the concept by demonstrating the fast self-propulsion velocity of the fabricated prototype during magnetic steering. The ultimate goal of this research is to realize an autonomous microrobot capable of performing medical tasks inside the human body. Many

issues remain, such as improving yield, controlling velocity, preventing adhesion to blood cells or vessels, avoiding rejection by the immune system, ensuring biocompatibility, and so on. Nevertheless, this concept has great potential as a configuration integrating energy supply, propulsion, and steering for microrobots operating in environments similar to biological fluids. Future medical applications expected for the self-propulsive microrobots with steering include a pulling mechanism to assist in guidewire insertion into blood vessels prior to catheter introduction, agents delivering drugs to dissolve blood clots, and so on. Such applications have the potential to improve the safety and reliability of many medical procedures.

REFERENCES

[1] R. A. Freitas Jr., *Nanomedicine Volume I. Basic Capabilities*. Georgetown, TX, USA: Landes Biosci., 1999.

[2] B. J. Nelson, I. K. Kaliakatsos, and J. J. Abbott, "Microrobots for minimally invasive medicine," *Annu. Rev. Biomed. Eng.*, vol. 12, pp. 55–85, 2010.

[3] S. Martel, "Microrobotics in the vascular network: Present status and next challenges," *J. Micro-Bio Robot.*, vol. 8, pp. 41–52, 2013.

[4] J. Li, B. Esteban-Fernández de Ávila, W. Gao, L. Zhang, and J. Wang, "Micro/nanorobots for biomedicine: Delivery, surgery, sensing, and detoxification," *Sci. Robot.*, vol. 2, no. 4, 2017, Art. no. eaam6431.

[5] S. T. Chang, V. N. Paunov, D. N. Petsev, and O. D. Velev, "Remotely powered self-propelling particles and micropumps based on miniature diodes," *Nature Mater.*, vol. 6, no. 3, pp. 235–240, 2007.

[6] M. Vonthron, V. Lalande, G. Bringout, C. Tremblay, and S. Martel, "A MRI-based integrated platform for the navigation of micro-devices and microrobots," in *Proc. IEEE/RSJ Int. Conf. Intell. Robots Syst.*, 2011, pp. 1285–1290.

[7] D. J. Bell, S. Leutenegger, K. M. Hammar, L. X. Dong, and B. J. Nelson, "Flagella-like propulsion for microrobots using a nanocoil and a rotating electromagnetic field," in *Proc. IEEE Int. Conf. Robot. Automat.*, 2007, pp. 1128–1133.

[8] A. Ghosh and P. Fischer, "Controlled propulsion of artificial magnetic nanostructured propellers," *Nano Lett.*, vol. 9, no. 6, pp. 2243–2245, 2009.

[9] Z. Wu, T. Si, W. Gao, X. Lin, J. Wang, and Q. He, "Superfast near-infrared light-driven polymer multilayer rockets," *Small*, vol. 12, no. 5, pp. 577–582, 2016.

[10] D. Ahmed et al., "Selectively manipulable acoustic-powered microswimmers," *Sci. Rep.*, vol. 5, no. 1, pp. 1–8, 2015.

[11] S. Martel, C. C. Tremblay, S. Ngakeng, and G. Langlois, "Controlled manipulation and actuation of micro-objects with magnetotactic bacteria," *Appl. Phys. Lett.*, vol. 89, no. 23, 2006, Art. no. 233904.

[12] S. Sanchez, A. N. Ananth, V. M. Fomin, M. Viehrig, and O. G. Schmidt, "Superfast motion of catalytic microjet engines at physiological temperature," *J. Amer. Chem. Soc.*, vol. 133, no. 38, pp. 14860–14863, 2011.

[13] W. F. Paxton, A. Sen, and T. E. Mallouk, "Motility of catalytic nanoparticles through self-generated forces," *Chem. Eur. J.*, vol. 11, no. 22, pp. 6462–6470, 2005.

[14] N. Mano and A. Heller, "Bioelectrochemical propulsion," *J. Amer. Chem. Soc.*, vol. 127, no. 33, pp. 11574–11575, 2005.

[15] X. Ma et al., "Enzyme-powered hollow mesoporous janus nanomotors," *Nano Lett.*, vol. 15, no. 10, pp. 7043–7050, 2015.

[16] E. Diller, J. Giltinan, and M. Sitti, "Independent control of multiple magnetic microrobots in three dimensions," *Int. J. Robot. Res.*, vol. 32, no. 5, pp. 614–631, 2013.

[17] T. Xu, C. Huang, Z. Lai, and X. Wu, "Independent control strategy of multiple magnetic flexible millirobots for position control and path following," *IEEE Trans. Robot.*, vol. 38, no. 5, pp. 2875–2887, Oct. 2022.

[18] C. Huang, T. Xu, and X. Wu, "Leader–follower formation control of magnetically actuated millirobots for automatic navigation," *IEEE/ASME Trans. Mechatron.*, early access, Aug. 10, 2023, doi: 10.1109/TMECH.2023.3300010.

[19] T. Yamanaka and F. Arai, "Self-propelled swimming microrobot using electroosmotic propulsion and biofuel cell," *IEEE Robot. Automat. Lett.*, vol. 3, no. 3, pp. 1787–1792, Jul. 2018.

[20] T. Yamanaka and F. Arai, "Miniaturization effect of electroosmotic self-propulsive microswimmer powered by biofuel cell," *Robomech J.*, vol. 6, no. 1, pp. 1–9, 2019.

[21] D. Jiles, *Introduction to Magnetism and Magnetic Materials*. Boca Raton, FL, USA: CRC, 2015.

[22] M. Suter et al., "Superparamagnetic photocurable nanocomposite for the fabrication of microcantilevers," *J. Micromechanics Microeng.*, vol. 21, no. 2, 2011, Art. no. 025023.

[23] M. Suter et al., "Superparamagnetic microrobots: Fabrication by two-photon polymerization and biocompatibility," *Biomed. Microdevices*, vol. 15, pp. 997–1003, 2013.

[24] X. Bao, A. Bontemps, S. Grondel, and E. Cattan, "Design and fabrication of insect-inspired composite wings for MAV application using MEMS technology," *J. Micromechanics Microengineering*, vol. 21, no. 12, 2011, Art. no. 125020.

[25] T. Sikanen, S. Tuomikoski, R. A. Ketola, R. Kostiainen, S. Franssila, and T. Kotiaho, "Characterization of SU-8 for electrokinetic microfluidic applications," *Lab Chip*, vol. 5, no. 8, pp. 888–896, 2005.

[26] T. Yamanaka and F. Arai, "Film-shaped self-powered electro-osmotic micropump array," *Micromachines*, vol. 14, no. 4, 2023, Art. no. 785.

[27] J. Weizenecker, J. Borgert, and B. Gleich, "A simulation study on the resolution and sensitivity of magnetic particle imaging," *Phys. Med. Biol.*, vol. 52, no. 21, 2007, Art. no. 6363.

[28] V. Soukharev, N. Mano, and A. Heller, "A four-electron O_2-electroreduction biocatalyst superior to platinum and a biofuel cell operating at 0.88 V," *J. Amer. Chem. Soc.*, vol. 126, no. 27, pp. 8368–8369, 2004.

[29] H. Bruus, *Theoretical Microfluidics*, vol. 18. London, U.K.: Oxford Univ. Press, 2007.

[30] E. Guazzelli and J. F. Morris, *A Physical Introduction to Suspension Dynamics*, vol. 45. Cambridge, U.K.: Cambridge Univ. Press, 2011.

[31] Z. Nagy, O. Ergeneman, J. J. Abbott, M. Hutter, A. M. Hirt, and B. J. Nelson, "Modeling assembled-MEMS microrobots for wireless magnetic control," in *Proc. IEEE Int. Conf. Robot. Automat.*, 2008, pp. 874–879.

[32] M. Beleggia, M. De Graef, and Y. Millev, "The equivalent ellipsoid of a magnetized body," *J. Phys. D: Appl. Phys.*, vol. 39, no. 5, p. 891, 2006.

[33] R. M. Murray and S. S. Sastry, "Nonholonomic motion planning: Steering using sinusoids," *IEEE Trans. Autom. Control*, vol. 38, no. 5, pp. 700–716, May 1993.

[34] M. Sampei, "A control strategy for a class of nonholonomic systems-time-state control form and its application," in *Proc. IEEE 33rd Conf. Decis. Control*, 1994, vol. 2, pp. 1120–1121.

[35] M. Sampei, H. Kiyota, H. Koga, and M. Suzuki, "Necessary and sufficient conditions for transformation of nonholonomic system into time-state control form," in *Proc. IEEE 35th Conf. Decis. Control*, 1996, vol. 4, pp. 4745–4746.

[36] S. D. Psoma, P. D. van der Wal, O. Frey, N. F. de Rooij, and A. P. Turner, "A novel enzyme entrapment in SU-8 microfabricated films for glucose micro-biosensors," *Biosensors Bioelectron.*, vol. 26, no. 4, pp. 1582–1587, 2010.